SEDIMENTS, SEC 3 · HILLSLOPE AND RIVER BASIN SEDIMENT DYNAMICS ·
RESEARCH ARTICLE

Tracking mineral and geochemical characteristics of Holocene lake sediments: the case of Hotagen, west-central Sweden

Hussein Jaafar Kanbar[1] · Thai Tran Le[1] · Fredrik Olajos[2] · Göran Englund[2] · Michael Holmboe[1]

Abstract

Purpose Intact lake sediments reflect the development of terrestrial ecosystems. This development can be understood by decoding mineral and geochemical information of sedimentary archives. Therefore, we characterized a Holocene lake sediment core and revealed bulk to micro-scale variations via a combination of geochemical techniques and statistical methods.

Methods A 2.3 m sediment core was collected from Hotagen, a lake in west-central Sweden; a sediment sample was collected every 5 cm. A part of each sediment sample was kept untreated (named bulk) and another part was size-fractionated into < 4, 4–16, 16–64, and > 64 μm subsamples. Characterization was then made with respect to grain size distribution (GSD), physico-chemical parameters, geochemical properties, organic composition, and mineralogy. The sediments were investigated at bulk, micro-, and elemental scales using powder X-ray diffraction (XRD), diffuse reflectance infrared Fourier transform spectroscopy (DRIFT), and scanning electron microscopy coupled to energy-dispersive X-ray spectroscopy (SEM–EDX).

Results The deepest sediment was identified as glacial till dating back to the Late Pleistocene. The bulk sediments showed a clear distinction between 0–195 cm (unit 1, U1) and 200–225 cm (unit 2, U2) depths. Quartz and feldspar minerals decreased and organic matter and clay minerals increased from the till towards the lower limit of U1. The development in the sedimentary properties marked the transformation of the terrestrial ecosystem from glacier-covered land to vegetated areas. This development was also well reflected by the appearance of X-ray amorphous materials and the formation of distinct organo-mineral aggregates; chlorite was the predominant clay mineral in these aggregates. The geochemical variation between U2 and U1 sediments was further established by resolving the DRIFT spectral components through multivariate curve resolution alternating least square (MCR-ALS). The U1 sediments settled over a period of ∼ 7500 years and showed comparable mineral, geochemical, and organic composition. However, the size-fractionated sediments, mainly < 4 μm, showed diverse mineral and geochemical composition. Indeed, these sediments were distinct by containing relatively higher amounts of X-ray amorphous materials and clay minerals, the latter had variable Na, Mg, and K contents.

Conclusion The combined use of geochemical and statistical approaches used in this study followed the mineral and geochemical development of sediments that had settled during the Late Pleistocene and Early Holocene Epochs. Finally, the U2 sediments marked the terrestrial ecosystem development that occurred during the late glaciation, deglaciation, and post-glaciation periods.

Keywords Sediment core · Size fraction · Post-glaciation · XRD · DRIFT · Ecosystem development

✉ Hussein Jaafar Kanbar
hsen.kanbar@gmail.com

✉ Michael Holmboe
michael.holmboe@umu.se

1 Department of Chemistry, Umeå University,
SE-901 87 Umea, Sweden

2 Department of Ecology & Environmental Sciences, Umeå
University, Umea, Sweden

1 Introduction

Lake sediments are recognized as storage zones for lithogenic and anthropogenic materials that are generated in catchments. These materials settle in lakes over long periods and form lacustrine archives (e.g., Schnurrenberger et al. 2003; Kalis et al. 2003). The inorganic and organic sedimentary composition reflect watershed lithology, terrestrial characteristics, ecosystem development, climate

change, mineralogy, and geochemical properties (e.g., Engstrom et al. 2000; Laceby et al. 2015; Panagiotopoulos et al. 2020; Strakhovenko et al. 2020). Therefore, lake sediment cores can reveal past environmental changes that had occurred approximately 10,000 years ago in Scandinavia during the transition from the Pleistocene to the Holocene Epochs (Mörner 2004; Stroeven et al. 2016). During the Late Pleistocene in Scandinavia, the Fennoscandian ice sheets eroded the landscape by plucking and abrasion, which resulted in fine clastic sediments. These fine sediments, as well as other clasts, rocks, and debris, were transported with glaciers and eventually settled when reaching lowland settings (Marshak 2011; Stroeven et al. 2016). Towards the Holocene, substantial changes occurred to the ecosystem as glaciers thawed, bedrock was exposed, and vegetation covered the land. Subsequently, primary producers facilitated weathering through the introduction of plant- and microbial-based organic acids.

Ecosystem development during the Pleistocene–Holocene transition and the Holocene can be revealed in sediments using organic proxies, such as pollen, micro- and macrofossils, and sedimentary ancient DNA (e.g., Pedersen et al. 2013; Capo et al. 2021), elemental proxies, such as carbon and nitrogen contents and isotopes (e.g., Pérez et al. 2014; Pulley et al. 2015), as well as mineral and geochemical ones (e.g., Alizai et al. 2012; Thorpe et al. 2019). The inorganic materials stored in sediments mainly reflect the catchment's bedrock, soil, and land cover. Therefore, sediments mark the development of terrestrial ecosystems and weathering magnitudes that were prominent during the Pleistocene–Holocene. Subsequently, more clay minerals and X-ray amorphous materials are enriched in fine sediments (Hillier 1995; Thorpe and Hurowitz 2020). The X-ray amorphous materials include allophanes, ferrihydrites, diatom frustules, and organic matter (Pérez et al. 2016; Thorpe et al. 2019). Those materials, in addition to clay minerals, (hydro)oxides, microorganisms, and organic matter (OM), represent cementing materials for aggregates (e.g., organo-mineral, mineral–mineral, and bio-organo-mineral). So, and due to increasing deposition of such phases, mainly during the Pleistocene–Holocene transition and the Holocene, aggregates are expected to form (e.g., Zimmermann-Timm 2002; Tombácz et al. 2004). The formation and size of aggregates depend on the mineral and organic composition (e.g., surface charge and area), as well as the physico–chemical conditions of the aqueous media (e.g., pH and ionic strength), water hydrodynamics, and turbulence (e.g., Lartiges et al. 2001; Tombácz et al. 2004; Bouyer et al. 2005; Tran and Strom 2019; Kanbar et al. 2020a). For example, distinct clay minerals (e.g., mica and chlorite minerals) are expected to behave differently in aggregates based on surface charge and area. Moreover, sedimentary organic matter reflects ecosystem development directly through its increasing deposition in lakes with time, especially after the Pleistocene,

and indirectly by the formation of organo-mineral aggregates (Schaaf et al. 2011). Vegetation covers bedrock and soil, thus reducing the erosion of particles and debris on the one hand, and promoting the erosion and weathering of fine particles on the other, such as clay minerals and X-ray amorphous materials. These changes can be monitored and studied through mineral and geochemical approaches.

To characterize mineral composition, variation, and evolution in sediment cores, powder X-ray diffraction (XRD) is commonly used. It is a fast and reliable technique to identify major crystalline minerals, quantify them using Rietveld refinement, and give indications about X-ray amorphous phases (e.g., Doebelin and Kleeberg 2015; Pérez et al. 2016; Thorpe et al. 2019). Additionally, infrared spectroscopy techniques, such as Fourier transform infrared (FTIR) and diffuse reflectance infrared Fourier transform (DRIFT), can reveal mineral (regardless of crystallinity), geochemical (or chemical), and organic characteristics of sediments. Indeed, infrared techniques proved to be fast, cheap, and effective techniques to study such characteristics (e.g., Madejová et al. 2017; Margenot et al. 2019). Using infrared techniques to reveal organic information has been proven to be accurate and faster in comparison to more time-consuming total organic carbon (TOC) or loss on ignition (LoI) measurements (Rosén et al. 2010; Ancin-Murguzur et al. 2020). Furthermore, DRIFT, and other vibrational spectroscopy data, can be treated by decomposing spectra into resolved components (Felten et al. 2019), which can then be used to detect minor mineral, chemical, and organic variations. Moreover, XRD and infrared techniques can be used in combination to follow changes in mineral properties, such as precipitation, intercalation of water molecules and ions, dissolution, swelling, and weathering (e.g., Lindholm et al. 2019; Kanbar and Kaouk 2019). Infrared spectroscopy is commonly used in connection to other geochemical techniques, such as XRD and electron microscopy, to reveal further information (e.g., Ammar et al. 2016; Le Meur et al. 2016). Scanning electron microscopy coupled to energy-dispersive X-ray (SEM-EDX) complements XRD and DRIFT by determining the elemental composition of particle surfaces. The variation in elemental composition, and more importantly elemental ratios, provided by SEM-EDX can detect minute elemental variations (Ewing and Nater 2003; Courtin-Nomade et al. 2015; Kanbar et al. 2017). Therefore, the combination of the abovementioned geochemical techniques can provide information at bulk, micro-, and elemental scales in sediments as well as other matrices (e.g., soils, technosols, polymers, and geo-polymeric materials). Hence, such analytical approaches are useful in studies where bulk and micro-scale variations are important to note, such as ecology, paleo-ecology, limnology, paleo-limnology, geology, and sedimentology.

The last glacial period in the northern hemisphere ended approximately 10,000 years ago. Subsequently, ecosystem

evolution prevailed during the late glaciation, deglaciation, and post-glaciation periods (e.g., Gibbard and Van Kolfschoten 2004; Öberg and Kullman 2011; Zimmermann et al. 2021). These changes are chronologically stored in undisturbed (intact) lacustrine sediments. The developments of the ecosystem during those periods have been recently recorded through sedimentary ancient DNA (sedaDNA) and organic proxies (e.g., Snowball et al. 2002; Zale et al. 2018; Zimmermann et al. 2021). Nonetheless, the mineral and geochemical composition of sediments that accompanied ecosystem development in Sweden, especially during the deglaciation and post-glacial periods, have not been reported. Therefore, this study aims to characterize the mineral, geochemical, and organic properties of sedimentary materials that have been deposited since the Late Pleistocene. This was done through a combination of geochemical techniques and statistical approaches that revealed information at different scales. Accordingly, bulk, micro-scale, and elemental analyses were carried out on initial and size-fractionated deposits of a sediment core.

2 Area description, sampling site, and sediment coring

A sediment core was collected from a lake in Hotagen, a tributary of the River Indalsälven, located in west-central Sweden (Fig. 1a). The watershed covers a 202-km² surface area and has an 850 mm average annual precipitation; its

land cover is dominated by boreal forests (~57%) and has very few urban areas (Fig. 1b). The catchment emerged from beneath the Fennoscandian ice-sheets approximately 10,000 years ago (Öberg and Kullman 2011; Stroeven et al. 2016). Due to limited anthropogenic activity in the region, the sediments in lake Hotagen are expected to reflect the Pleistocene–Holocene transition that occurred during the late-glaciation, deglaciation, and post-glaciation periods. The sediment core was collected from the smaller basin called Laxviken (east part of the lake) which was covered by a 20-m water column; the maximum depth in the lake was 71 m. The sampling area is located in the Caledonian orogen and the bedrock is mainly composed of graywacke, granite, quartz arenite, granitoid, feldspathic metasandstone, amphibolite, phyllite, and limestone (Fig. 1c) (ESDAC - European Commission 1963; Andersson et al. 1985; SGU 2019). Consequently, the main mineral composition of the bedrock is quartz, amphiboles, chlorites, alkali feldspars, plagioclase feldspars, mica, calcite, aragonite, and dolomite.

The 2.3 m sediment core was collected using an 86-mm inner-diameter piston corer (Olajos et al. 2018). The top 6 cm of the core was not collected due to possible disturbance of the loose and muddy surface sediments during coring. Therefore, the depths indicated in this study are in reference to the uppermost sediment (i.e., 6 cm below the top of the core).

Fig. 1 a Overview map of part of northern Europe (modified from Feher (2020)), b land cover map showing the main land cover classes (Corine Land Cover 2018) and the watershed's boundary (https://vattenwebb.smhi.se/hydronu/), and c geological map showing the main bedrock composition (SGU 2019). The location of the sediment core is indicated by arrows
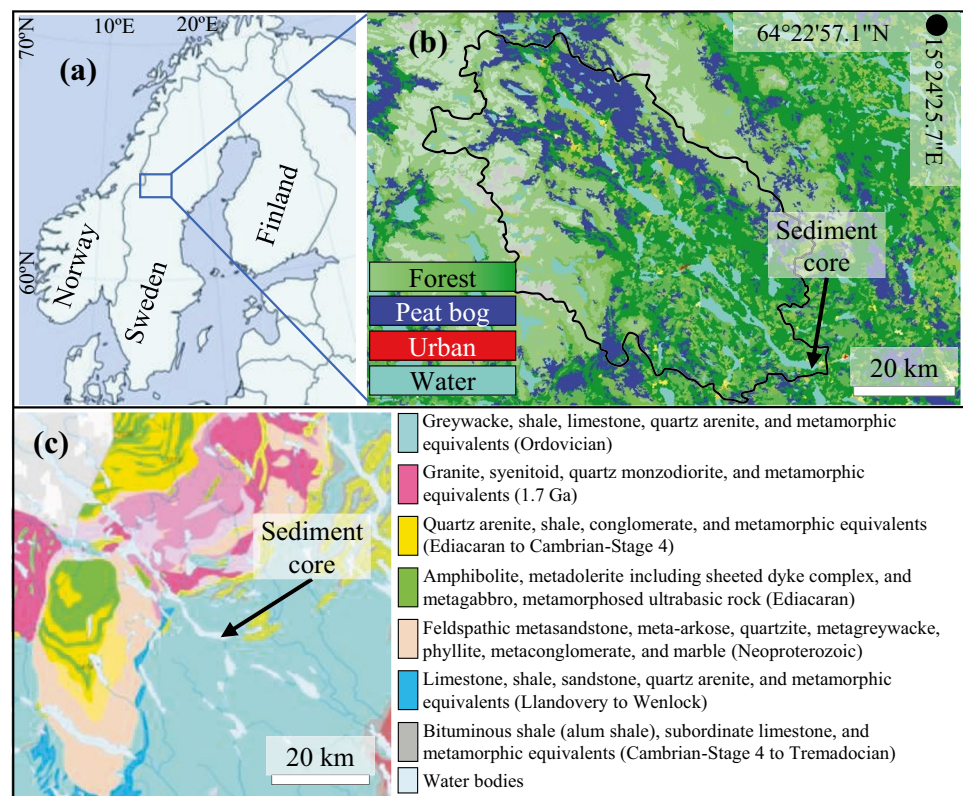
3 Materials and methods

3.1 Sample preparation, size fractionation, and treatment

Radiocarbon dating was done to three wood macrofossils that were found at different depths in the core using an accelerator mass spectrometry (AMS) at the Beta Analytic Radiocarbon Dating Laboratory, Miami Florida. The depth estimates were translated to age estimates using the R-based program Clam 2.2 (Blaauw 2010). For mineral and geochemical analyses, a sediment sample was collected every 5 cm along the 2.3 m core. The sediments on the periphery of the core were discarded due to possible lateral movement during coring. Each of the 45 samples was divided into two parts, an intact and untreated part (named bulk) and a size-fractionated part (having sizes of <4, 4–16, 16–64, and >64 μm). Before fractionation via particle settling (using Stokes' Law, e.g., see Bergaya and Lagaly (2013)), the samples were mixed in ultrapure water overnight. To maintain the characteristics of the sediment fractions, the aggregates (organo-mineral and mineral–mineral) were not disaggregated. This was an important part because DNA sorption was assessed on lake Hotagen sediments based on the geochemical, mineral, and organic compositions of each size fraction, including the aggregates (Kanbar et al. 2020b). Therefore, each size fraction contained aggregates of the relatively smaller fraction(s), except the <4 μm fraction, i.e., the clay-sized fraction, since it is the smallest one. Unless indicated otherwise, the bulk and size-fractionated sediments were freeze-dried and ground, using an agate mortar and pestle, before analyses.

It is worth noting that all the bulk sediments were characterized by XRD and DRIFT ($n = 45$). Due to similar mineral and geochemical compositions throughout large parts of the core (as described later in the text), size-fractionated samples of selected sediment depths were chosen for further investigation. Additionally, elemental composition (by X-ray fluorescence, XRF), cation exchange capacity (CEC), and pH were determined for selected bulk sediments (SM 1).

3.2 Grain size distribution

Grain size distribution (GSD) analysis was performed on the bulk sediments by laser diffraction (Partica LA-950V2 laser scattering particle size distribution analyzer from Horiba). The samples were neither freeze-dried nor disaggregated prior to GSD analysis. The bulk sediments were mixed in a sample bath with distilled water and grain size measurements were done before and after applying sonication for 1 min. Measurements were done before and after sonication

to study aggregate size. Non-sonicated measurements indicate aggregate sizes (or sediment sizes), while measurements after sonication indicate grain sizes (or particle sizes), as sonication breaks aggregates.

3.3 Powder X-ray diffraction

The crystalline minerals of the bulk and size-fractionated sediments were identified by randomly-oriented powder X-ray diffraction (XRD) measurements using PANalytical X'pert[3] diffractometer (CuKα radiation 1.54187 Å). The ground sediments were front-loaded onto 16 mm stainless-steel circular cavity holders and were run using a spinner stage (for better randomization) with the following parameters: 4–64° 2θ, 0.026° step size, 1 s collecting time, 4 s/spin, 45 kV, 40 mA, 0.04 rad Soller slits, 1/8° incident divergence slit, 5 mm anti-scattering receiving slit, and 10 mm mask. The crystalline minerals were identified with the HighScore Plus software (Degen et al. 2014) and the Crystallography Open Database (COD), and then quantified from the experimental diffractograms by Rietveld refinement using Profex-BGMN (Post and Bish 1989; Doebelin and Kleeberg 2015; Döbelin 2021) and structural data from the COD. For accurate peak shape modeling, the fundamental parameters approach (FPA) was set to match the instrument's configurations (e.g., divergence slits, Soller slits, and optical elements in the beam path), and the parameters k2 (micro-strain broadening), B1 (crystallite size), and GEWICHT (scale factor that quantifies the phase's weight fraction in the sample as well as corrects preferred orientation) were refined. Subsequently, the goodness-of-fit (GoF) and chi-squared values (χ^2) were used to assess the quality of the fit (Döbelin 2021); the χ^2 and GoF values are reported in SM 2. To verify the reproducibility of mineral quantification due to sample preparation (i.e., mounting and possible preferred orientation), two sets of samples were mounted and measured four times and gave similar results (SM 2).

For selected bulk sediments, oriented mounts were prepared on glass slides to characterize clay minerals using the protocol developed at the Laboratoire Interdisciplinaire des Environnements Continentaux (LIEC), Nancy, France (Bihannic and Gley 2021). Due to similar clay mineral composition in all the sediments, two samples were chosen for oriented XRD measurements. Briefly, the sediments were disaggregated via sonication and the particles smaller than 4 μm were collected by applying Stokes' law. These clay-mineral rich suspensions were then transferred to three glass slides and left to settle with preferred orientation along the c-axis. The samples were air-dried, treated with ethylene glycol, and calcinated at 550 °C. The vapor treatment was used for the ethylene glycol-treated samples (e.g., Poppe et al. 2001). Subsequently, XRD measurements were done with the following parameters: 3–30° 2θ, 0.016° step size, 1.7 s collecting time, 45 kV, 40 mA, 0.04 rad

Soller slits, 1/8° incident divergence slit, 5 mm anti-scattering receiving slit, and 10 mm mask.

3.4 Diffuse reflectance infrared Fourier transform spectroscopy

Diffuse reflectance infrared Fourier transform spectroscopy (DRIFT, IFS 66v/s by Bruker) was used to determine the functional groups of all bulk and selected size-fractionated sediments. Well-homogenized and dry mixtures of sediments were prepared with KBr for DRIFT measurements. For each sample, 128 spectra were recorded under vacuum (<7 mbar) in the 5200–400 cm^{-1} range with a 4 cm^{-1} spectral resolution. In order to decompose the complex multi-component spectra into pure phase components, the raw infrared (IR) spectra were treated using the open-source MCR-ALS GUI (multivariate curve resolution alternating least square gentle user interface) provided by the Vibration Spectroscopy Core Facility at Umeå University (Felten et al. 2015, 2019; www.umu.se/en/research/infrastructure/visp/downloads/). Multiple regression was used to estimate the organic matter contents based on LoI (calculated from XRF) and organic IR signatures (e.g., Rosén et al. 2010). Loss on ignition or organic matter content was calculated by the complementarity of the sum of major oxides to 100; this method has been shown to accurately represent sedimentary organic matter in various lakes (Rydberg 2014).

3.4.1 Chemical and mineral identification of sediments after organic matter removal

Sedimentary organic matter was chemically removed by sodium hypochlorite (NaOCl) from the same samples that were analyzed by XRD and DRIFT; this method was used since it does not modify mineral structures, unlike ashing and H$_2$O$_2$ treatment (e.g., Mikutta et al. 2005; Margenot et al. 2015). Detailed information on organic matter removal by NaOCl can be found elsewhere (Margenot et al. 2019 and SM 3). The sediments subjected to organic matter removal are hereafter denoted Sed$_{inorg}$, indicating the inorganic nature; non-treated sediments are denoted Sed. The Sed$_{inorg}$ samples (bulk and size-fractionated) were then analyzed by DRIFT. Consequently, and due to the disappearance of OM IR peaks which partly interfere with mineral IR peaks, some of the DRIFT chemical and mineral fingerprints were clearer for Sed$_{inorg}$ in comparison to Sed.

3.5 Scanning electron microscopy

A scanning electron microscopy coupled to energy-dispersive X-ray spectroscopy (SEM-EDX) was used to investigate the elemental composition of the predominant mineral surfaces

(Carl Zeiss Evo SEM with LaB6 electron source, UCEM). Non-metal coated dry sediments were mounted onto double-adhesive carbon tapes and measured under low vacuum conditions (LV, 60 Pa). Quantitative EDX spectra were collected using Aztec 3.3 (Oxford instruments) with dead time below 10%, EDX signals between 8000 and 10,000 counts/s, and using oxygen for stoichiometry and carbon as a deconvolution element (not used in elemental quantification).

4 Results

4.1 Sediment age, accumulation, size, and aggregation

The deepest sediment (225 cm) dated to the Late Pleistocene, approximately 10,000 years ago, and was identified as glacial till that had deposited during the end of the glacial period (Fig. 2a). This sediment had a distinct gray color. The color then faded into a brown color just above the till (i.e., at depth 220 cm) until 180 cm. No noticeable color variation was seen for the 0–180 cm sediments, except for a lighter brown color for the 1, 5, 35, and 135 cm sediments. The color transformation in the till-180 cm reflects a change in the sedimentary materials that had settled during approximately 2000 years (Fig. 2a). Due to limited human interference in the area, the sediments are unlikely to have been dredged or disturbed. The sediment accumulation rate in the lake ranged between 0.19 and 0.37 mm/yr, as inferred by the three AMS radiocarbon dates (Fig. 2a). The summary of the radiocarbon dates is included in Table 1 and the calibration of radiocarbon ages to calendar ages is included in SM 4. The sediment accumulation rates roughly indicate that each 5 cm, the distance between the sampled sediments in the core, is a product of 125–250 years of deposition. The relatively low sedimentation rates are likely due to the small catchment area, low primary production as a result of cold and nutrient-poor environments (Olli 2008; Lawson et al. 2012), and the presence of larger lakes upstream of the sampling site that function as sedimentation basins.

The sediment sizes did not show a clear trend as a function of depth (Fig. 2b). Nonetheless, there is a noticeable pattern every ~25 cm, as indicated in the <4 μm fractions (e.g., 20–45, 90–110, and 170–200 cm; Fig. 2b and SM 5a). The abundance of the 4–16-μm fraction varied slightly with depth in comparison to the other fractions. The till had approximately 50% of sedimentary materials coarser than 64 μm. Moreover, even without disaggregation (e.g., sonication), the samples showed a considerable fraction below 4 μm (5–42%), indicating an overall clayey nature of the sediments.

Fig. 2 a Sediment age-depth model with 95% confidence interval (shaded area) and average sedimentation rates, **b** sediment size based on Stokes' law (dashed arrows indicate patterns; explained in the text), and **c** grain size distribution (GSD) of bulk sediments with non-sonicated samples in black (representing aggregates) and sonicated samples in red (representing grains or particles); the cylinder represents the sediment core and follows the same vertical scale as part "**a**" of this figure. Each plotted profile represents the GSD of one sediment sample, where the number of sediment samples is 9 and 3 for 0–180 and 200–212 cm, respectively
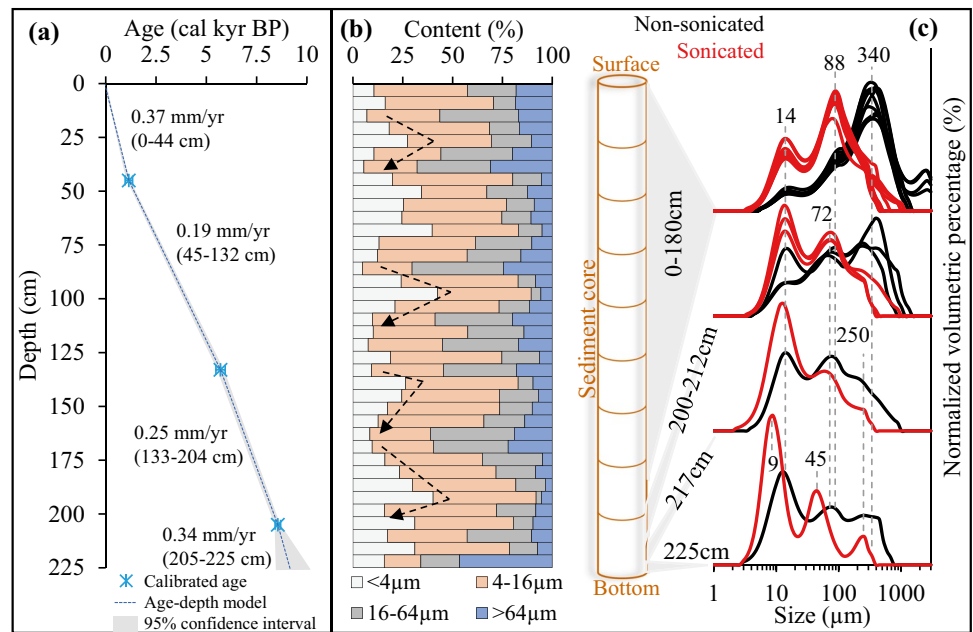
The bulk sediments showed multimodal GSD (Fig. 2c). Based on the sonicated (representing grain or particle sizes) and non-sonicated samples (representing aggregate or sediment sizes), the sediment core can be divided into distinct sections, which correspond to 0–180 cm, 200–212 cm, 217 cm, and 225 cm (till). For the sonicated samples, the till particles were predominantly centered at 9 μm, followed by relatively coarser 45 μm (silty) and 250 μm (fine-medium sand) populations. This coarsest population was also reflected by a relatively high >64 μm fraction (Fig. 2b). From the till towards later sediments (i.e., sediments that had settled afterward), the finest population shifted towards coarser sizes, i.e., from 9 μm in the till to 12 μm in 217 cm and to 14 μm in 200–212 cm and 0–180 cm (Fig. 2c). The 45-μm population of the till behaved in a similar manner; it increased to 62, 72, and 88 μm in the 217 cm, 200–212 cm, and 0–180 cm sediments, respectively. The non-sonicated samples also showed a gradual size increase from the till towards later sediments (Fig. 2c). Indeed, there is a clear shift of the predominant sediment population from the till (14 μm) towards the 0–180 cm sediments (340 μm). Also, the coarse populations of the non-sonicated samples shifted

to smaller sizes upon sonication; these smaller populations were already observed in the sediments (non-sonicated), but became more obvious after sonication. For example, the 14 and 88 μm populations of the 0–180 cm sediments were slightly visible in the non-sonicated samples, but became clear after sonication. This indicates that those particles were initially present as aggregates, possibly organo-mineral and mineral–mineral aggregates. Therefore, it is expected that these sediments, i.e., 0–180 cm, contain higher amounts of cementing materials (such as organic matter, carbonates, and clay minerals). Furthermore, the variation between aggregate and particle sizes is more significant in the 0–180 cm sediments, while it was reduced in the underlying 200–212 cm sediments, and relatively insignificant in the 217 and 225 cm sediments. This shows that more aggregations had formed during the later stages of the Holocene, i.e., in the 0–180 cm sediments that had settled in the last ~7500 years (Fig. 2a, c). Finally, the GSD profiles shifted from finely skewed in the 0–180 cm sediments to symmetrical and coarsely skewed in the deepest sediments, and the till showed to be very poorly sorted in comparison to the other sediments (based on Blott and Pye (2001), SM 5b).

Table 1 Summary of the radiocarbon data obtained from the sediment core

Sediment depth (cm)	Sample ID (Beta Lab ID*)	[14]C age (BP) ± 1σ	Calibrated age range (BP)	Dating material
45	Beta-517571	1220 ± 30	1258–1063	Wood
133	Beta-517572	4980 ± 30	5862–5612	Wood
205	Beta-517573	7780 ± 30	8609–8455	Wood

*The permanent sample ID assigned by Beta Analytic Inc

4.2 Bulk sediments

4.2.1 Crystalline mineralogy as a function of depth

Lake Hotagen sediments were mainly composed of silicate minerals, such as quartz, amphiboles (inosilicates), feldspars (tectosilicates), and clay minerals (phyllosilicates), which were present throughout the core (Fig. 3a). Amphibole minerals were mainly identified by the diffraction peak at 8.4 Å. The XRD patterns and watershed's lithology suggest that the amphibole mineral is tremolite, yet it cannot be easily distinguished from actinolite or hornblende, which are constituents of the parent bedrock in the watershed. Therefore, the mineral(s) identified by the 8.4 Å peak will be addressed as amphibole. The phyllosilicate minerals detected in the sediments were chlorite and mica, as mainly identified by the 14- and 10 Å diffraction peaks, respectively. The 7.14- and 3.58 Å peaks could be assigned to kaolinite (001 and 002 reflections, respectively) as well as chlorite (002 and 004 reflections, respectively). However, kaolinite did not appear to be present in the sediments due to the absence of the 060 peak at 1.50 Å. Further explanation is included in the oriented XRD patterns (SM 6). The 10- and 5 Å diffraction

peaks belong to micaceous minerals, such as illite, muscovite, and biotite. The relative broad 001 peak suggests illite since muscovite and biotite have relatively sharper 001 peaks. Nonetheless, due to the common origin and complexity of clear mineral identification in heterogeneous sediments, and based on lithology, biotite, and muscovite might also be present. Indeed, such micaceous minerals result from glacial grinding which can further form illite (Poppe et al. 2001; Galán 2006). Therefore, these minerals will be addressed as mica minerals. Additionally, the phyllosilicates were further noted by the diffraction peaks at 4.5, 2.6, and 1.54 Å (Fig. 3a). The 060 reflections between 1.50 and 1.54 Å, as in this case, indicate tri-octahedral phyllosilicates, while di-octahedral silicates have the 060 reflections between 1.48 and 1.50 Å (Brown and Brindley 1980). All these minerals, in addition to quartz (3.34 Å) and feldspars, originated from the parent bedrock (Fig. 1c) as suggested by the watershed's lithology (SGU 2019). The feldspar minerals identified in the sediments were Na-feldspars (albite, 3.19 Å), K-feldspars (orthoclase and microcline, ~3.2 Å), and possibly Na, K-feldspars (anorthoclase, ~3.2 Å). Due to the heterogeneity of the sediments, the feldspar minerals will be addressed as albite (Na-feldspars) and K-feldspars. Unlike

Fig. 3 **a** XRD patterns of bulk sediments. Ch, chlorite; M, mica; Am, amphibole; Phyl, phyllosilicates; Q, quartz; P, pyrite; Fld, feldspars; K-fld, K-rich feldspars (orthoclase and microcline); and Al, albite. The inset to the right highlights the change in quartz and feldspar peaks. **b** Mineral contents of the bulk sediments as a function of depth
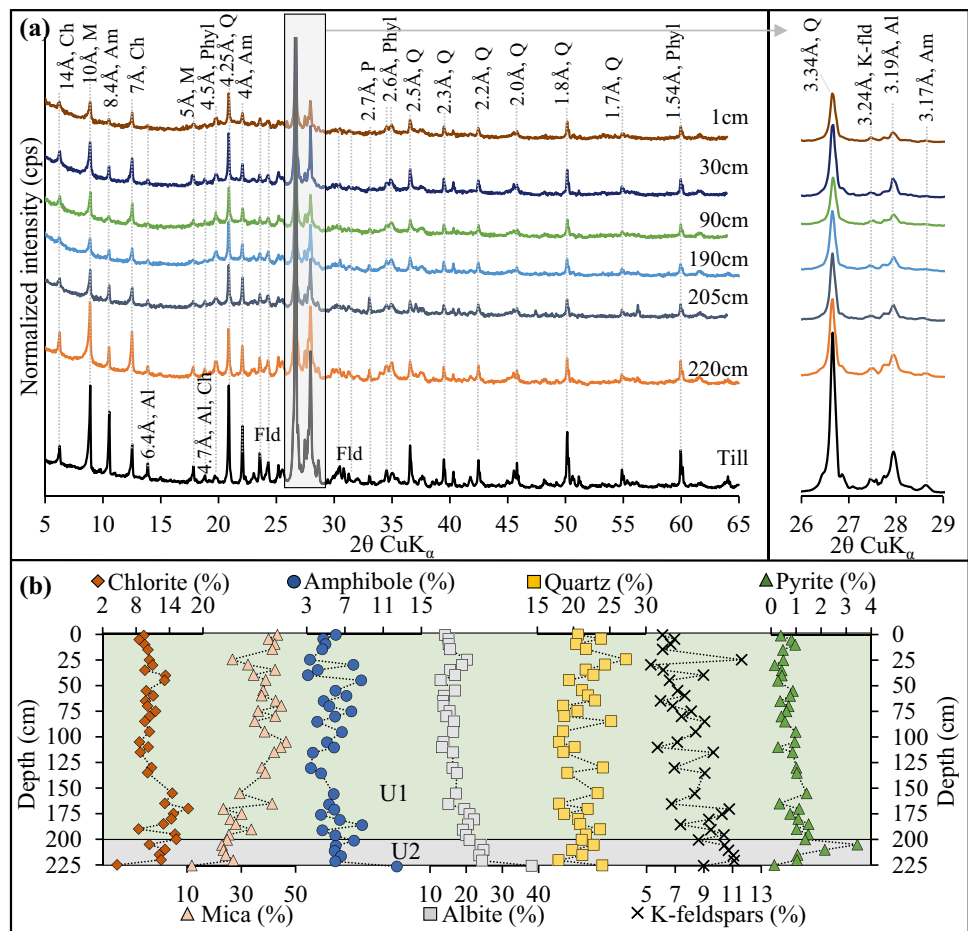
the other minerals, pyrite (2.7 Å) was mainly detected in sediments below 190 cm (Fig. 3a). Although the watershed contains carbonate bedrock, no crystalline carbonates were detected by XRD (e.g., aragonite, calcite, or dolomite); swelling clay minerals were also not detected. More information about sheet silicates obtained from oriented XRD patterns is included in SM 6. Furthermore, the diffractogram of the 220 cm sediment showed a small bump in the 15–25° 2θ region (Fig. 3a). This bump gradually increased towards 210 cm and appeared to be similar for the rest of the sediments. The bump indicates X-ray amorphous materials, such as allophanes, diatoms, and organic matter (Pérez et al. 2016; Thorpe et al. 2019).

Quartz, mica, and albite minerals were predominant throughout the core, while chlorite, amphibole, and K-feldspar minerals were less abundant; pyrite was only detected in certain sediments (Fig. 3b). The abundance of quartz (24%), albite (38%), and amphiboles (13%) in the till reflected the watershed's lithology (ESDAC - European Commission 1963; Andersson et al. 1985; SGU 2019). Above the till (i.e., 220 cm), these minerals were less abundant and phyllosilicates (chlorite and mica) were more prominent. Mica mineral contents increased from the till towards 200 cm, whereas albite showed an opposite trend. Based on those minerals, it is clear that the till is distinct, the 200–220 cm sediments showed unique trends, and the overlying and younger 0–195 cm sediments showed variable mineral composition. Amphibole minerals did not display a depth-dependence trend; pyrite generally increased from 225 to 205 cm and then decreased and was negligible throughout the core. According to the XRD findings, the sediments can

be categorized into unit 1 (U1 0–195 cm) and unit 2 (U2 200–225 cm). Even though GSD suggested more distinct sections (Fig. 2c), the last three sections (i.e., 200–212, 217, and 225 cm) can be considered as the transition from the till towards the more homogeneous U1 sediments. More information about sediment categorization is included later in the text and in SM 7.

4.2.2 Mineral, chemical, and organic variation as a function of depth: DRIFT

The IR spectra of the bulk sediments showed chemical variations mainly among the U2 sediments on the one hand, and between the U1 and U2 sediments on the other (Fig. 4a). These variations reflect the composition of various minerals and are mainly based on the Si–O stretching and bending vibrations in the 1200–950- and 600–400 cm^{-1} regions, respectively, and on the OH stretching and bending vibrations (of silicates and aluminosilicates) in the 3700–3500- and 950–650 cm^{-1} regions, respectively (Fig. 4a). The OH stretching peaks of kaolinite octahedral layers (at 3697 and 3620 cm^{-1}) were absent, thus confirming the XRD findings that kaolinite is not present in the sediments. The Si–O stretching peaks identified at 1095 and 1020 cm^{-1} were attributed to silicate minerals, such as quartz, feldspars, and phyllosilicates (Parikh et al. 2014; Madejová et al. 2017). Due to the heterogeneity of the bulk sediments, i.e., they contain all these minerals (Fig. 3), the assignment of the peaks to their respective minerals was not possible. Quartz was readily identified in the till by the quartz overtone combination bands at 1995, 1875, and 1790 cm^{-1} as well as 1685, 1612, and 1525 cm^{-1} (Nguyen et al. 1991; Padilla et al. 2014).

Fig. 4 a DRIFT spectra of bulk sediments. The U1 sediments (0–195 cm) are marked in blue and the U2 sediments (200–225 cm) are marked in black-gray, except the till, which is marked in red; 220 cm is marked in black and the color changes to lighter gray for the above U2 sediments. The spectra in the 1300–400 cm^{-1} region are stacked for clearer visualization of the Si–O peak shift (1095–1020 cm^{-1}). The inset shows the variation of organic matter (OM) with depth. **b** The resolved MCR-ALS spectral components of the bulk sediments (C1 and C2 are component 1 and component 2, respectively) and **c** the resolved concentration profiles of the two components
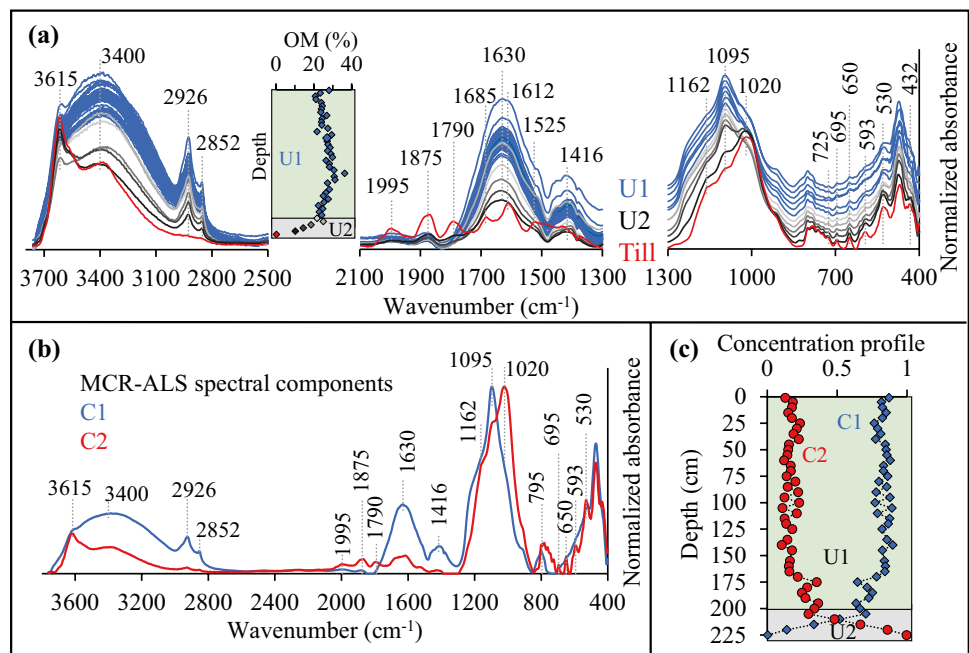
Some of these bands were obvious in the till due to the absence of the overlapping OM peak at 1630 cm⁻¹. Furthermore, the till showed the Si–O stretching peak at 1020 cm⁻¹ and a shoulder at 1095 cm⁻¹ (red spectrum in Fig. 4a). The shoulder at 1095 cm⁻¹ then protruded into a peak in the 220 cm sediment, and eventually two peaks were seen in 215 cm (i.e., at 1020 and 1095 cm⁻¹). The overlying sediments (i.e., 0–210 cm) had the Si–O stretching peak predominantly at 1095 cm⁻¹ and a shoulder at 1020 cm⁻¹. Additionally, the 0–215 cm sediments showed a shoulder at 1250–1170 cm⁻¹, suggesting quartz, humic substances, allophanes, amorphous silicates, or diatom frustules (Rosén et al. 2010; Meyer-Jacob et al. 2014). The change in the OH and Si–O bending vibrations in the 800–690 cm⁻¹ and 600–400 cm⁻¹ regions, respectively, evolved like the Si–O stretching bands (i.e., from the till towards 215 cm). This suggests that these chemical signatures are related to the same minerals. Moreover, the intensity and position of the OH stretching and water bending vibrations (~3400 and 1640 cm⁻¹, respectively) are affected by interlayer cations (Madejová et al. 2017 and references therein), indicating a change in the abundant mineral(s), especially between the U1 and U2 sediments.

As for the organic IR signature, the variation was based on the peaks at 3400 cm⁻¹ (amine N–H stretching and OH stretching of humic substances), 2926 and 2852 cm⁻¹ (aliphatic C–H stretching), 1630 cm⁻¹ (aromatic C=C stretching and/or amide C=O), 1614 cm⁻¹ (–C–O stretching in carboxyl groups of humic substances; –COOH), and 1416–1400 cm⁻¹ (aliphatic C–H bending) (Parikh et al. 2014; Madejová et al. 2017). The link between these peaks and organic matter content has been described elsewhere (e.g., Rosén et al. 2010). Furthermore, the bands at 3400 and 1640 cm⁻¹ also indicate OH stretching and bending of water molecules, respectively. These organic IR signatures were quasi-absent in the till which contained only 0.27% organic matter (inset in Fig. 4a and SM 1). The organic matter contents increased from the till to the U1–U2 transition region at 195–200 cm (except for 205 cm) and fluctuated between 20 and 35% in the U1 sediments. Moreover, the main IR variation of the U1 sediments was due to OM. This is supported by similar DRIFT spectra for the U1 sediments after OM removal, i.e., for Sed$_{inorg}$, as indicated by MCR-ALS (SM 8).

Two MCR-ALS spectral components explained the variation of the bulk sediments throughout the core (Fig. 4b), each representing a distinct mineral and geochemical composition. The MCR-ALS approach was used to decompose the experimental IR spectra by first computing the most probable number of pure components by single value decomposition, and secondly by finding the pure spectral components and their respective weights, which are shown as concentration profiles (Fig. 4c). It should be noted that the changes within the U2 sediments, as seen by GSD, XRD, and DRIFT (Figs. 2c, 3b, and 4a), can further be divided into more MCR components; this is

addressed when size-fractionated sediments are discussed (Section 4.3.2). The MCR spectral component C1 was characterized by the presence of organic matter (according to the peaks described in the previous paragraph) and an Si–O stretching peak at 1095 cm⁻¹ (Fig. 4b); C2 was distinct by lacking OM bands and having unique peaks at 1020 cm⁻¹ (Si–O stretching), 800–600 cm⁻¹ (OH bending), 600–400 cm⁻¹ (Si–O bending), and 2000–1600 cm⁻¹ (quartz overtone). The first MCR spectral component (C1) predominated the 0–205 cm sediments, as indicated by the resolved MCR-ALS concentration profile (Fig. 4c). However, this signature gradually declined from 175 towards 210 cm, where the latter sediment had almost equal contributions of C1 and C2. Subsequently, the MCR component C2 predominated the deepest sediments (215–225 cm).

4.3 Size-fractionated sediments

4.3.1 Crystalline mineralogy based on sediment size

In most U1 sediments, the <4 and 4–16 μm size fractions and the 16–64- and >64-μm size fractions showed distinct mica, albite, and quartz mineral contents; mica minerals were enriched in the former fractions while albite and quartz were enriched in the latter fractions (Fig. 5a). As for chlorite, although enriched in the <4 μm fractions in some sediments (e.g., 5, 25, 110, and 170 cm), it did not show a clear enrichment in the finest sediment fractions as mica did. Furthermore, the distinction of minerals based on size-fractions did not necessarily apply in the U2 sediments. For instance, albite and mica mineral contents were distinct between the <4 μm fractions on the one hand and the >4 μm fractions on the other (i.e., 4–16, 16–64, and >64 μm). Clay minerals, as well as organic matter, are part of cementing materials for aggregates and are therefore included in the coarse fractions (Fig. 2c). Thus, clay minerals are not necessarily enriched in the fine fractions. Amphibole mineral contents were lowest in the <4 μm sediments, while the other size fractions showed fluctuating contents. Nonetheless, more amphibole was detected in the U2 sediments with increasing size fractions. Pyrite and K-feldspar contents did not show a clear trend with sediment size. Pyrite showed a noticeable increase from the till towards 205 cm, as mainly seen in the <4 μm sediments. Interestingly, the finest fraction of the till displayed similar mineral characteristics to the 16–64- and >64-μm fractions of the U1 sediments, e.g., mica, amphibole, and albite (Fig. 5a). The X-ray amorphous materials indicated by the bump in the 15–25° 2θ region were more noticeable in the U1 sediments in comparison to the U2 sediments (Fig. 5b). Moreover, this signature was higher for the <4 μm fractions in comparison to the coarser fractions (4–16, 16–64, and >64 μm); the latter showed similar bump signatures. Similar to the bulk sample, the size-fractionated till samples did not display a bump in that region (Fig. 5b).
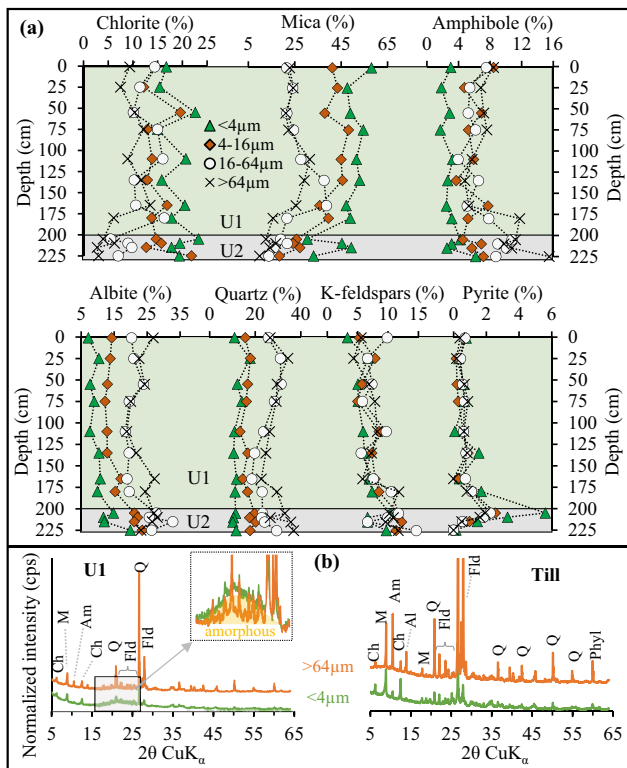
Fig. 5 **a** Mineral composition of the size-fractionated sediments as a function of depth and **b** X-ray diffractograms of < 4 and > 64 μm size fractions for 1 cm (representing U1) and the till; both diffractograms have the same Y-axis scale. Ch: chlorite, M: mica, Am: amphibole, Q: quartz, Fld: feldspars. The inset shows the bump that indicates X-ray amorphous materials; the diffractograms are superimposed for clearer visualization of the bump. All peaks and d-spacings are included in Fig. 3

4.3.2 Mineral, chemical, and organic variation based on sediment size: DRIFT

Bulk samples showed the distinction between U1 and U2 sediments (Figs. 3 and 4). Therefore, MCR-ALS analyses of the size-fractionated sediments were done for these two units separately. Accordingly, the MCR-ALS results showed the geochemical variations firstly based on sediment size and secondly on depth. Two MCR spectral components explained the IR variation in the U1 sediments (Fig. 6a). The first MCR component applied to the < 4 μm fractions of all the U1 sediments and showed an Si–O peak at 1095 cm^{-1} and had relatively low OM IR signatures. Therefore, the Si–O stretching peak at 1095 cm^{-1} was assigned to clay minerals (chlorite and/or mica in this case). Additionally, the shoulder at ~1200 cm^{-1} was more obvious for the < 4 μm fractions (inset in Fig. 6a), suggesting higher contents of amorphous materials in that fraction. This was also evidenced by the bump in the X-ray diffractograms (Fig. 5b). The second MCR spectral component was characterized by

an additional Si–O stretching peak at 1020 cm^{-1} and relatively high OM and quartz overtone peaks (insets in Fig. 6a). This component applied to the fractions greater than 4 μm (i.e., 4–16, 16–64, and > 64 μm). In the U1 sediments, the resolved MCR components were easily distinguished between < 4 μm (C1) and > 4 μm (C2) sediment, but they did not change as a function of depth. Therefore, the concentration profile is not shown.

The U2 sediments showed geochemical variations based on size fraction as well as depth. The size-fractionated U2 sediments showed three resolved MCR spectral components (Fig. 6b). The first component (C1) mainly described the till and to a lesser extent 215 cm (Fig. 6c). This component was characterized by a clear Si–O peak at 1020 cm^{-1}, quartz peaks (1995–1525 cm^{-1}), specific bands at 950–650 cm^{-1}, and the absence of OM IR signatures, and predominantly applied to all the till fractions (Fig. 6c) since the quartz overtone peaks were clearly visible (Fig. 6d). The second MCR component (C2) was characterized by two Si–O peaks (1095 and 1020 cm^{-1}, inset in Fig. 6b), relatively high OM peaks, and some quartz overtone peaks. This component mainly described the 205 cm sediments greater than 4 μm. The bulk 205 cm sediment showed relatively high OM content as well (Fig. 4a); it is worth noting that the high OM IR signatures,
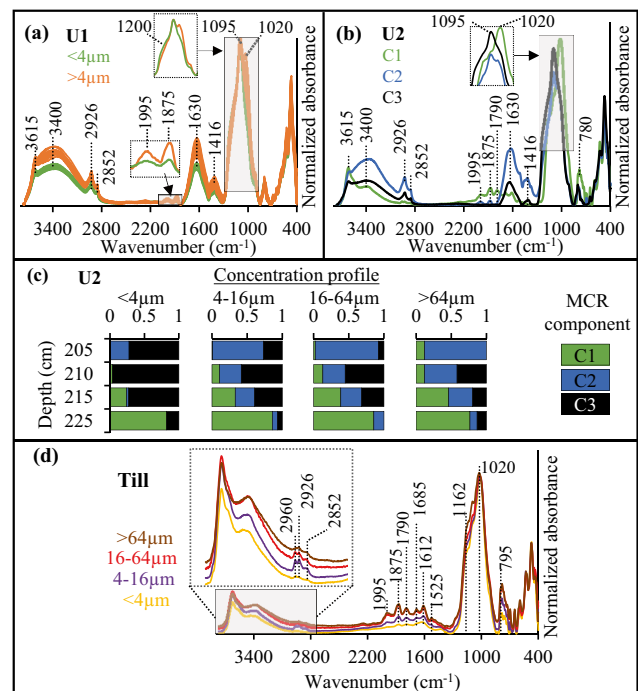

Fig. 6 **a** DRIFT spectra of the U1 sediments showing the distinction between < 4 and > 4 μm size fractions (indicating the two MCR spectral components). **b** The MCR spectral components and **c** concentration profiles of the size-fractionated U2 sediments. **d** The DRIFT spectra of the size-fractionated till with focus on the OM peaks (inset)

in this case, might have overwhelmed the signatures of the other MCR components. The third MCR component (C3) showed a relatively sharp Si–O peak at 1095 cm^{-1}, the absence of quartz overtone peaks, and small OM peaks; this component predominantly described the <4 µm fractions of the U2 sediments except the till. Furthermore, the <4 µm fraction of the till showed comparable IR peaks to the coarser fractions of the other sediments, i.e., quartz overtone peaks at 2000–1600 cm^{-1} and an Si–O stretching peak at 1020 cm^{-1} (Fig. 6a, d).

The change in the predominance of C1 in the till to C3 in 210 cm and then C2 in 205 cm highlights the evolution of the sediments (Fig. 6c). Indeed, the MCR components showed the transition from OM-depleted and quartz and feldspar-rich samples (represented by C1, Fig. 6b), to sediments with relatively moderate OM and clay mineral contents (C3), and finally to OM-rich and clay mineral-rich samples (C2). The component C2 held the characteristics of the U1 sediments (Fig. 6a, b), regardless of size. According to these components, such as the presence of the Si–O peak at 1020 cm^{-1} in the till and in the coarse fractions of the other sediments, and in combination with XRD findings, this peak was assigned to feldspar and/or quartz. Feldspar was also characterized by the 950–650 cm^{-1} and 725 cm^{-1} fingerprints and quartz was identified by the bands between 2000 and 1800 cm^{-1} (Padilla et al. 2014; Meyer-Jacob et al. 2014). The change in quartz and/or feldspar on the one hand, and clay mineral peaks (1020–1095 cm^{-1}) on the other, was seen in the bulk U2 sediments (Fig. 4a). The Si–O bending (at 593, 530, and 432 cm^{-1}) and OH bending (at 725, 695, and 650 cm^{-1}) vibrations also identified feldspar minerals in the coarse U2 sediments. These are the characteristics of C1 (Fig. 6b) which decreased from the till towards 180 cm (Fig. 4a). Interestingly, the till showed organic matter signatures in the 3000–2800 cm^{-1} region (inset in Fig. 6d). Nonetheless, the intensities of these OM peaks were significantly lower than any other sediment in the core. In addition to the 2852 and 2926 cm^{-1} OM IR peaks that were detected in all the other sediments, the till showed a unique peak at 2960 cm^{-1} (indicating aliphatic C–H groups of organic matter), which was mainly detected in the 4–16 µm fraction.

4.4 Micro-scale variation: SEM–EDX

The elemental composition of the predominant mineral surfaces in the sediments (i.e., aluminosilicates: feldspar and clay minerals) was addressed at micro-scale levels using SEM-EDX (Fig. 7). Morphologically, the SEM images showed well-aggregated phases, even in the finest fractions (Fig. 7a), and relatively large particles in the >64 µm fractions (Fig. 7b). Regardless of sediment depth or size fraction, Si was the major element, followed by Al, and then Fe, Mg, Na, and K, while Ti, S, and P were only detected in trace amounts (EDX spectra in Fig. 7). Within the same sediment depth, the

elemental composition varied based on size fraction (e.g., the <4 and >64 µm fractions of 1 cm in Fig. 7a, b, respectively), which reflected mineral variation. The aluminosilicates in the <4 µm fractions contained higher Si contents and lower Al, Fe, Ca, K, Na, and Mg contents than the >64 µm fractions (Fig. 7a, b). This variation was consistent throughout similar phases within each sample, as compiled in Table 2. Furthermore, the change in the main elemental ratios, i.e., Si/Al, pointed to this variation. Indeed, the Si/Al ratios averaged 6.9 (±1.8) and 2.4 (±0.2) in the <4 µm and >64 µm fractions, respectively (Table 2). Similar to the mineral and geochemical variations identified by XRD and DRIFT (Figs. 5 and 6), the elemental composition of the <4 µm fraction of the till was comparable to the >64 µm sediments of U1 (Fig. 7b, d). Yet, the till was more enriched in Al, Na, Mg, and K, contained less Si, and consequently had lower Si/Al ratios (Table 2). The enrichment of these cations in the fine fraction of the till reflected the predominance of feldspar minerals and cation-rich aluminosilicates such as albite (Figs. 3b and 5a). In addition to the predominant aluminosilicates, some less significant minerals were identified, such as framboidal pyrite (SM 9) and zinc sulfide (Fig. 7b); pyrite was identified in the finest fractions of U2 (Fig. 5b). Diatom frustules were detected throughout the sediment core except the till (Fig. 7a–c).

5 Discussion

5.1 Tracking sedimentary characteristics using a combination of geochemical techniques: application in this study and perspectives

The data obtained from the various geochemical techniques showed similar categorization of the bulk sediments. The sediments were divided into two units with inflection points roughly at 200 cm based on XRD (Fig. 3b) and OM (Fig. 4a), and at 210 cm based on DRIFT (Fig. 4c). In fact, more dissimilar categorization was expected since these techniques yield distinct findings; XRD mainly gives information on crystalline minerals while DRIFT considers chemical, organic, and mineral signatures (regardless of crystallinity). The similarity in the categorization of the sediments strongly suggests that the mineral and organic evolution occurred conjointly as a result of ecosystem development that had occurred in the late glaciation, deglaciation, and post-glaciation periods. Indeed, natural environmental changes that occurred during these periods can lead to such changes (e.g., Snowball et al. 2002; Voldstad et al. 2020; Zimmermann et al. 2021).

The application of the MCR-ALS GUI was initially intended for biological material (Felten et al. 2015, 2019). However, it showed significant findings when applied to the mineral, organic, and geochemical data in this study. Hence, this technique advances the categorization and interpretation of sediment

Fig. 7 SEM back-scattered electron (BSE) micro-images for sediments. **a** Fine surface sediment (< 4 μm, case of 1 cm, U1) showing (1) aluminosilicates, (2) Mg-rich aluminosilicate, and (3) diatom frustule. **b** Coarse surface sediment (> 64 μm, case of 1 cm, U1) showing (4) aluminosilicates, and (5) zinc sulfide. **c** Diatom frustules were generally found in the sediments throughout the core except the till. **d** Fine fraction of the till (< 4 μm, 225 cm, U2) showing (6) aluminosilicates. Numbers on the images show where EDX spectra were collected; the EDX spectra next to the images belong to the data points marked with asterisks. Due to the similarity in elemental composition (A, %), the same number is assigned to similar phases (in each image). The average elemental composition of these points is included in Table 2. The carbon emission lines in the EDX spectra belong to carbon tape onto which the samples were deposited; carbon was not taken into consideration upon elemental quantification
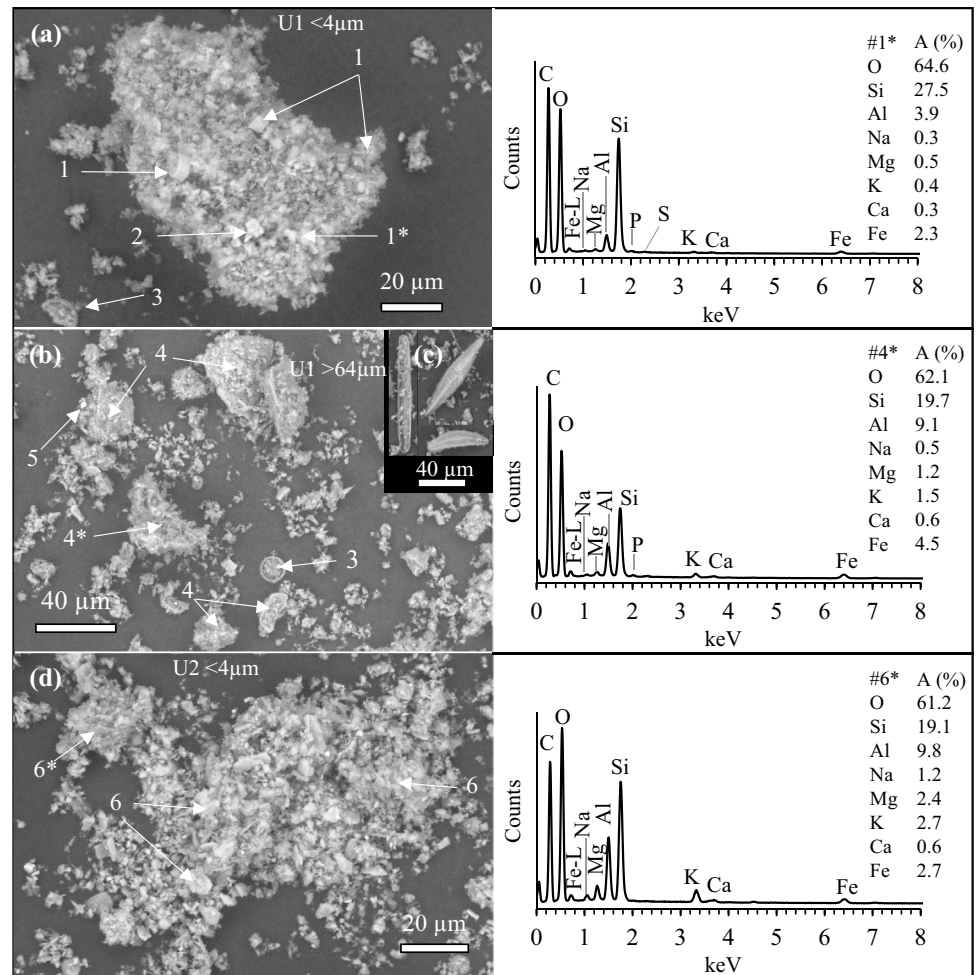
properties, which is crucial in fields where sediment or soil cores are studied (e.g., paleo-limnology, paleo-ecology, sedimentology, and landscape ecology). Furthermore, the DRIFT data covered the mineral and organic variations of the sediments, which were further improved by linking it to XRD. For instance, amorphous materials were detected by a bump in the diffractograms (~15–25° 2θ; Figs. 3a and 5b) and by a shoulder in the IR spectra (~1200 cm^{-1}; Figs. 4a and 6a). In both techniques (i.e., XRD and DRIFT), these signatures were more obvious in the U1 sediments and the <4 μm fractions in comparison to the U2 sediments and the coarser fractions. Similar to using IR signatures as a fast, reliable, and cost-effective tool to semi-quantify total organic carbon, carbonates, and biogenic silica (e.g., Rosén et al. 2010; Ancin-Murguzur et al. 2020), IR might be used to quantify amorphous materials in heterogeneous environmental matrices, such as sediments and soils (e.g., Pérez et al. 2016). It should be noted that whether the amorphous material(s) detected in both techniques are the same has not been established. Either way, such findings would be less tedious and more timesaving than the conventional methods of amorphous phase quantification by XRD using internal standards (e.g., Zhou et al. 2018; Thorpe et al. 2019).

5.2 First sedimentary materials reaching the lake after the glacial period

Deglaciation in Fennoscandia occurred between 22,000 and 9700 years BP (Mörner 2004; Stroeven et al. 2016). During that period, mountainous areas witnessed steepening, degradation, and collapse of rockwalls, subsequently generating rock debris (Ballantyne 2002; Jarman 2002) that deposited and formed unsorted glacial sediments, i.e., the till (e.g., Hall et al. 2019). Indeed, the till in lake Hotagen was very poorly sorted (SM 5b) and reflected the lithogenic character of the watershed by high quartz (24%), albite (38%), and amphibole (12%) contents (Fig. 3). The till had a finer texture in comparison to the other sediments (Fig. 2c), possibly due to harsh mechanical weathering (e.g., grinding) that resulted from glacial abrasion during deglaciation (Riebe et al. 2004). Additionally, this weathering process also homogenized the sediments and made mineral variation per size fraction less obvious in comparison to the other sediments (Fig. 5a); this also explains the enrichment of feldspar minerals in the fine fraction of the till, whereas these minerals were abundant in the coarse fractions of the

Table 2 The atomic composition of the aluminosilicates in the three sediment samples presented in Fig. 7; n=4, 5, and 4 for U1 <4 µm, U1 >64 µm, and U2 <4 µm, respectively

	Atomic percentage (%)								Ratio
	O	Si	Al	Na	Mg	K	Ca	Fe	Si/Al
U1 <4 µm	64.5 ± 0.5	27.1 ± 1.3	4.1 ± 0.8	0.2 ± 0.1	0.5 ± 0.1	0.6 ± 0.2	0.3 ± 0.1	2.4 ± 0.5	6.9 ± 1.8
U1 >64 µm	62.0 ± 0.3	20.3 ± 0.5	8.4 ± 0.6	0.8 ± 0.8	0.9 ± 0.3	2.0 ± 1.3	0.6 ± 0.3	4.4 ± 1.5	2.4 ± 0.2
U2 <4 µm	60.9 ± 0.4	19.1 ± 1.2	9.1 ± 0.7	1.4 ± 0.8	2.5 ± 0.5	2.8 ± 0.6	0.6 ± 0.2	3.2 ± 0.9	2.1 ± 0.2

other sediments (Fig. 5a). Moreover, the <4 µm fraction of the till and the >64 µm fractions of the other sediments showed similar geochemical characteristics, such as the presence of quartz overtone peaks, an Si–O stretching peak at 1020 cm^{-1}, and Si–O and OH bending peaks (Fig. 6). Furthermore, the bulk and size-fractionated till did not show signatures of X-ray amorphous materials (Figs. 3a and 5b). This indicates the absence of materials such as organic matter, allophanes, and diatom frustules on the one hand, and/or the limitation or absence of chemical weathering of silicate minerals on the other.

Organic matter IR signatures were identified mainly in the 4–16 and 16–64 µm fractions of the till (Fig. 6d). This OM might have been preserved in ice-sheets, possibly in interglacial soils that deposited during deglaciation and post-glaciation, or might have come from organisms that formed during the Late Pleistocene (late glaciation or deglaciation periods) or Early Holocene (e.g., Zale et al. 2018; Zimmermann et al. 2021). Indeed, it was shown that vegetation was able to penetrate thin ice sheets during Late glaciation 14,000–11,000 years ago (Kullman 2002). However, the OM IR peak at 2960 cm^{-1} was only detected in the till, and not in the other sediments. This suggests that the unique OM IR band belongs to material(s) that was stored in ice-sheets that thawed in the vicinity of lake Hotagen, was present pre-deglaciation and discontinued post-glaciation (e.g., Clarke et al. 2019; Zimmermann et al. 2021), or originated from another watershed (e.g., Sadori 2013). Radiocarbon dating, organic identification, pollen records, and sedimentary ancient DNA can give more information in this regard (e.g., Öberg and Kullman 2011; Swärd et al. 2018). Although the dating records were only based on three wood samples, the sedimentation rate was higher in the 205–225 cm sediments in comparison to the above 133–205 cm sediments (Fig. 2a). Relatively higher sedimentation rates are due to paraglacial landscape response, i.e., the absence of vegetation, high discharge, and elevated erosion and transportation of deposits (e.g., Ballantyne 2002), which are thought to have predominated during the Late Pleistocene (late glaciation and deglaciation periods) and Early Holocene (post-glaciation).

5.3 Sedimentary materials marked ecosystem development during the Late Pleistocene–Holocene

Primary succession evolved during the Late Pleistocene–Early Holocene due to deglaciation, which caused biological, chemical, and physical changes to the ecosystem (e.g., Engstrom et al. 2000; Ballantyne 2019). Terrestrial and aquatic vegetations subsequently increased OM deposition in lakes (Righi and Meunier 1995), as shown by the gradual increase in sedimentary OM in the U2 sediments (Fig. 8a). Furthermore, the gradual change from glacier-covered land (during late glaciation–deglaciation), to bare soil and exposed bedrock (deglaciation–post-glaciation), and eventually vegetated land (Holocene) caused a variation in the materials that were transported in the watershed and finally reached lakes. Such organic and inorganic changes were noted as a function of sediment size and depth (Figs. 3, 4, 5, and 6). Based on the watershed's bedrock and soil coverage in west-central Sweden, the predominant minerals are amphibole, quartz, feldspar, chlorite, and mica (Andersson et al. 1985; Allen et al. 2001; SGU 2019). The sum of quartz, albite, and K-feldspars on the one hand (i.e., the minerals that predominated the coarse fraction) and the sum of the clay minerals (i.e., chlorite and mica minerals that predominated the fine fraction) and OM on the other hand showed opposite trends with depth (Fig. 8a). These trends suggest that OM and mineral variation conjointly reflect ecosystem development. Also, the U2 sediments showed the transition from glacially derived sediments to more common lacustrine sediments, represented by the drastic changes from the till to the overlying U2 sediments (Figs. 3, 4, 5, and 6).

Pyrite might have also reflected the watershed's development (e.g., through change in land cover). Pyrite contents gradually increased from the till to 205 cm (Fig 3b). Since the Fe contents in the sediments were relatively low, pyrite is thought to have been inherited from parent bedrock rather than being formed within the sediments (e.g., Ohfuji and Rickard 2005). So, the variation in pyrite contents might be due to change in land cover (from exposed bedrock to vegetated areas) or modification in the particles that reached the lake as a result of size-dependent transportation caused by vegetation. The latter case might be plausible since pyrite was significantly enriched in

the <4 μm size fractions of the U2 sediments, while it showed similar contents in the other fractions (Fig. 5a). Carbonates were not detected in the sediments despite their presence in the bedrock (SGU 2019); the absence of crystalline carbonates was established by XRD (Fig. 3a). Furthermore, it is clear to say that these minerals, if present, were not below the XRD detection limit since they could not be detected by SEM-EDX. In this case, the bedrock containing carbonates might not have been exposed and therefore could not be transported to the lake, or carbonates were dissolved as a result of weathering (e.g., Hanna et al. 2018). Although the former might be more plausible, the latter cannot be ignored due to the acidic pH of the sediments and nearby lakes (SM 1).

The absence of X-ray amorphous materials in the till and their presence in the overlying sediments reflected ecosystem change as well (Figs. 3a and 5b). This change was marked by increasing contents of clay minerals and organic matter (especially between the till and the overlying U2 sediments, Fig. 8a), however, it might also be due to increased contents of allophanes, ferrihydrites, diatom frustules, and weathered silicate minerals (Pérez et al. 2016; Thorpe et al. 2019). Sedimentary aggregates also indicate ecosystem development (e.g., Schaaf et al. 2011). Indeed, sedimentary aggregates showed twofold variations in our case. The first is the gradual increase in the difference between aggregate and particle sizes from the till to the overlying sediments (Fig. 2c). The second variation was noted as a function of depth; with time, larger aggregates were detected in the sediments. The main aggregate size population shifted from 14 μm in the till, to 72 and 250 μm in the other U2 sediments, and finally to a clear 340 μm population in all the U1 sediments (Fig. 2c). Both variations are linked to higher contents of cementing materials, which are clay minerals, OM, and X-ray amorphous phases (Fig. 8a). These materials were enriched in the U1 sediments that showed the highest difference between particle and sediment sizes on the one hand, and the biggest aggregate sizes on the other (Fig. 2c). Although not studied here, microorganisms are also linked to aggregate formation via biofilms (Lartiges et al. 2001; Zimmermann-Timm 2002). Therefore, sedimentary aggregates and their composition can be used as proxies to study ecosystem development. Aggregates are affected by river hydrodynamics (e.g., turbulence), physico-chemical properties of the media (e.g., pH, redox conditions, and ionic strength), and suspended matter concentration (e.g., Tran and Strom 2019). Therefore, the trend in aggregate size of the <4 μm fraction (Fig. 2b) might be connected to such parameters.

5.4 More insights into ecosystem development through size-fractionated sediments and correlations

The size-fractionated sediments showed a clear variation between OM, the sum of quartz and feldspar minerals, and the sum of clay minerals (Fig. 8b). This was primarily seen between the till and the other sediments (red symbols in Fig. 8b) and secondly between the U1 and U2 sediments, and reflects ecosystem development marked by important mineral, organic, and geochemical transformations. The U2–U1 transition was recorded in terms of GSD, mineral, organic, chemical, and elemental compositions (Figs. 2c, 3b, 4c, and 8). Unfortunately, the till-220 cm transformation was not well-recorded in this study since sediments were collected every 5 cm; sampling at smaller intervals would have shown this transition better. However, among the different size fractions, the increase in quartz and feldspar minerals and decline in clay minerals was gradually observed with increasing sediment sizes, yet it was more significant between the <4 μm fraction and the other fractions combined (Fig. 8b); OM variation was only observed between the <4 and >4 μm size fractions, as established by multivariate analysis (Fig. 6a).

The correlation of the mineral and organic properties of the sediments by principal component analysis (PCA) highlighted ecosystem development (Fig. 8c). The first principal component (PC1) explained 41.9% of the variance with positive loadings for quartz, albite, amphibole, and to a lesser extent K-feldspars, and negative loadings for the clay minerals (the correlation matrices and PCA components are included in SM 10). The second component (PC2) described 34.9% of the variance and is directly related to organic matter. As discussed in the previous section, the transformation of those variables marked the changes within the U2 sediments and between U2 and U1 sediments. Moreover, there is a link between the quartz IR data and quartz contents from XRD (Fig. 8c and SM 10). It should be noted that the quartz DRIFT fingerprint was obtained from Sed_{inorg} samples since organic matter bands interfere with parts of the quartz fingerprint (at 1525 cm^{-1}). This correlation was valid for the quartz IR peaks at 1995, 1791, 1875, and 1525 cm^{-1}, but not for 1612 and 1685 cm^{-1} (Fig. 8c and SM 10). Indeed, recent studies used quartz IR fingerprints, mainly the Si–O stretching and bending vibrations, to quantify quartz in sediments (Vogel et al. 2016; Hahn et al. 2018).

The aluminosilicates in the <4 μm fractions showed variable elemental composition based on four groups, which are 1 cm, 25 and 165 cm, 220 cm, and the till (Fig. 8d). Therefore, even though the sediments were categorized into two units based on major mineral and geochemical characteristics, more distinction was possible at micro-scales. The decline in cations (sum of Na, Mg, and K) from the till towards 220 cm indicated, at least partially, the transition from cation-rich aluminosilicates (e.g., K-feldspar and albite) to mica and chlorite minerals. This transition was more obvious between U2 (220 and 225 cm) and U1 (25 and 165 cm), i.e., when significant sedimentary variation occurred. Interestingly, the abundance of the major cations and ratios did not change in U1, except for the surface
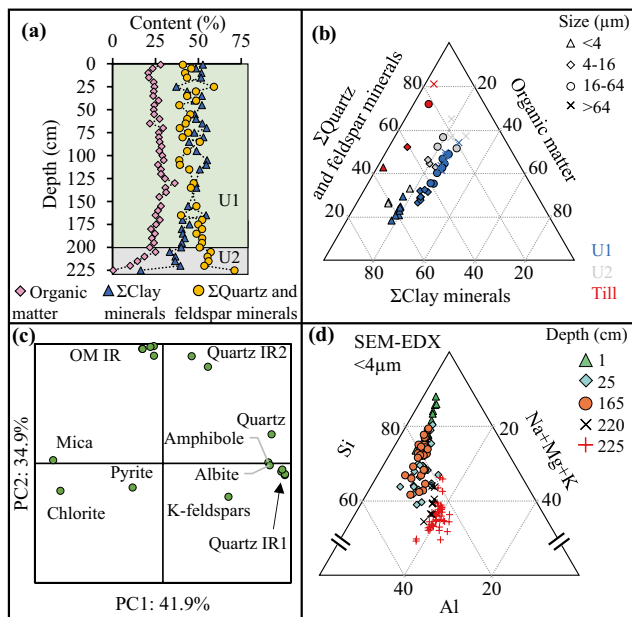
Fig. 8 Change of OM, the sum of clay minerals (mica and chlorite), and the sum of quartz and feldspar minerals (K-feldspars and albite) for **a** bulk sediments as a function of depth and **b** size-fractionated sediments (n = 12 for each size fraction). **b** The U1 sediments (0–195 cm) are marked in blue and the U2 sediments (200–225) are marked in gray, except the till, which is marked in red; each symbol represents a size fraction. **c** Principal component analysis (PCA) matrix for the sediments (bulk and size-fractionated); n = 60 for each variable. The data points represent the mineral percentages (XRD-Profex) except for those marked by IR, which were taken from DRIFT data. OM IR represents the DRIFT intensity peaks at 1416, 1630, 2852, 2927, and 3400 cm^{-1}. Quartz IR1 and Quartz IR2 represent the DRIFT intensity peaks at 1525, 1790, 1875, and 1995 cm^{-1}, and 1612 and 1685 cm^{-1}, respectively; since OM interferes with some quartz IR peaks, the quartz IR data were taken from Sed$_{inorg}$ samples, i.e., sediments after OM removal. d) Atomic abundance (SEM–EDX) of the < 4 μm fractions of 1, 25, 165, 220, and 225 cm sediments, with n = 19, 32, 25, 8, and 46, respectively

sediment (Fig. 8d). The similarity in the elemental composition of the predominant mineral surfaces in U1 (e.g., 25 and 165 cm) suggests that insignificant mineral variation occurred over a period of roughly 6400 years, i.e., the period during which these sediments had deposited.

In general, the most weathered minerals and mineraloids, such as clay minerals, poorly crystalline minerals, and amorphous materials, are enriched in fine sediments (e.g., Velde and Meunier 2008; Thorpe et al. 2019). Despite the prevailing cold climate conditions in Hotagen that limit chemical weathering and although we did not directly prove that chemical weathering occurred, the enrichment of possibly weathered materials in the < 4 μm sediments, i.e., clay minerals and X-ray amorphous material (Fig. 5), suggest chemical weathering of silicates. Indeed, chemical weathering was proven to be possible in conditions similar to this study (Thorpe

et al. 2019). In any case, X-ray amorphous materials and clay minerals promote aggregate formation. The formation and size of aggregates depend on surface charge and area of the aggregate-forming materials (e.g., Tombácz and Szekeres 2006). Since chlorite minerals have higher surface charges than mica minerals, chlorite is expected to be the predominant clay mineral in the organo-mineral or mineral–mineral aggregates (Poirier et al. 2020), followed by mica. Interestingly, this was noticeable based on chlorite and mica contents in the different size fractions. Unlike mica, chlorite was not noticeably enriched in the fine fraction (Fig. 5a). Additionally, and in contrast to mica, the difference in chlorite contents between the size fractions was not clear. This strongly suggests that chlorite is the main clay mineral involved in the aggregates. Indeed, it has been statistically proven that mica minerals had more available reactive sites than chlorite, since the latter was part of organo-mineral and mineral–mineral complexes (Kanbar et al. 2020b).

Finally, the combined use of the geochemical techniques, i.e., XRD, DRIFT, and SEM-EDX, and statistical approaches showed sedimentary variations at different scales. Firstly, XRD showed bulk variation in mineralogy, which was used to track major ecosystem changes that occurred during the Late Pleistocene–Early Holocene. This was mainly seen by the change in the abundance of crystalline minerals, the appearance of X-ray amorphous materials (Figs. 3 and 5), and the formation of aggregates (Fig. 2c). Secondly, DRIFT showed mineral, chemical, and organic variations (Fig. 4), which better marked the transition during the deglaciation and post-glaciation periods. Moreover, applying MCR-ALS to the size-fractionated sediments tracked sedimentary evolution with depth as well as sediment size (Fig. 6a–c). Finally, SEM-EDX further identified micro-scale variations of the predominant minerals (Fig. 8b).

6 Conclusion

A 2.3 m sediment core collected from lake Hotagen, west-central Sweden, revealed ~10,000 years of ecosystem development that occurred after the last glacial period. The bulk sediments were categorized into two distinct units based on grain size distribution (GSD), bulk mineralogy (XRD), chemical and organic compositions (DRIFT), and micro-scale analyses (SEM-EDX). The first unit (0–195 cm, U1) presented similar mineral and organic characteristics at a bulk scale and the second unit (200–225 cm, U2) marked the development of the catchment during the Late Pleistocene–early Holocene (i.e., during late glaciation, deglaciation, and post-glaciation). The mineral variation was marked by decreasing quartz, feldspar, and amphibole contents and increasing organic matter and clay mineral contents (mica and chlorite) with time. The chemical and organic variations were

clearly shown by multivariate analysis (MCR-ALS) of the DRIFT spectra that further showed distinct subunits. Indeed, the organic and mineral transitions within the U2 sediments and between U1 and U2, especially for the size-fractionated sediments, reflected the progression of the ecosystem post-glaciation. Ecosystem development was also denoted by the development of X-ray amorphous materials as well as the formation of distinct organo-mineral and mineral–mineral aggregates. Chlorite was proven to be the predominant clay mineral included in these aggregates. Furthermore, SEM-EDX revealed micro-scale variations (Na, K, and Mg) of the predominant aluminosilicates. The U1 sediments were shown to be different only at the micro-scale, while the U2 sediments were different at the mineral, chemical, organic, and micro-scales. Additionally, the 0–195 cm sediments, which had deposited over a period of roughly 7500 years, showed similar mineral and organic characteristics. This suggests that the sedimentary materials mainly changed during the early stages of the Pleistocene–Holocene transition that are archived in the U2 sediments. Only minor elemental changes occurred once major ecosystem development ceased, i.e., when organic deposition in the sediments reached a constant level. The geochemical techniques used in this study, especially when applied to the clay-sized fractions, demonstrated bulk, micro-, and elemental scale variations that marked mineral, organic, and elemental progression of the sediments as the ecosystem evolved post-glaciation.

Declarations

References

Alizai A, Hillier S, Clift PD et al (2012) Clay mineral variations in Holocene terrestrial sediments from the Indus Basin. Quat Res 77:368–381. https://doi.org/10.1016/j.yqres.2012.01.008

Allen CE, Darmody RG, Thorn CE et al (2001) Clay mineralogy, chemical weathering and landscape evolution in Arctic - Alpine Sweden. Geoderma 99:277–294. https://doi.org/10.1016/S0016-7061(00)00075-6

Ammar R, Kanbar HJ, Kazpard V et al (2016) Role of phosphogypsum and NPK amendments on the retention or leaching of metals in different soils. J Environ Manage 178:20–29. https://doi.org/10.1016/j.jenvman.2016.04.042

Ancin-Murguzur FJ, Brown AG, Clarke C et al (2020) How well can near infrared reflectance spectroscopy (NIRS) measure sediment organic matter in multiple lakes? J Paleolimnol 64:59–69. https://doi.org/10.1007/s10933-020-00121-5

Andersson A, Dahlman B, Gee DG, Snall S (1985) The Scandinavian Alum Shales. Sveriges geologiska undersökning

Ballantyne CK (2002) Paraglacial Geomorphology. Encycl Quat Sci Second Ed 21:553–565. https://doi.org/10.1016/B978-0-444-53643-3.00089-3

Ballantyne CK (2019) After the ice: lateglacial and holocene landforms and landscape evolution in Scotland. Earth Environ Sci Trans R Soc Edinburgh 110:133–171. https://doi.org/10.1017/S175569101800004X

Bergaya F, Lagaly G (2013) Purification of natural clays. In: Bergaya F, Lagaly G (eds) Handbook of clay science. Part A: Fundamentals, 2nd edn. Elsevier, pp 213–242

Bihannic I, Gley R (2021) Diffraction des rayons X sur poudres. https://liec.univ-lorraine.fr/content/fiche-diffraction-rayons-x. Accessed 26 Mar 2021

Blaauw M (2010) Methods and code for 'classical' age-modelling of radiocarbon sequences. Quat Geochronol 5:512–518. https://doi.org/10.1016/j.quageo.2010.01.002

Blott SJ, Pye K (2001) GRADISTAT: a grain size distribution and statistics package for the analysis of unconsolidated sediments. Earth Surf Process Landforms 26:1237–1248. https://doi.org/10.1002/esp.261

Bouyer D, Coufort C, Liné A, Do-Quang Z (2005) Experimental analysis of floc size distributions in a 1-L jar under different hydrodynamics and physicochemical conditions. J Colloid Interface Sci 292:413–428. https://doi.org/10.1016/j.jcis.2005.06.011

Brown G, Brindley GW (1980) X-ray diffraction procedures for clay mineral identification. In: Brindley GW, Brown G (eds) Crystal structures of clay minerals and their X-ray identification. Mineralogical Society, London, pp 305–359

Capo E, Giguet-Covex C, Rouillard A et al (2021) Lake sedimentary DNA research on past terrestrial and aquatic biodiversity: Overview and recommendations. Quaternary 4:6. https://doi.org/10.3390/quat4010006

Clarke CL, Edwards ME, Brown AG et al (2019) Holocene floristic diversity and richness in northeast Norway revealed by sedimentary ancient DNA (sedaDNA) and pollen. Boreas 48:299–316. https://doi.org/10.1111/bor.12357

Corine Land Cover (2018) CLC 2018 — Copernicus Land Monitoring Service. https://land.copernicus.eu/pan-european/corine-land-cover/clc2018?tab=mapview. Accessed 13 Feb 2020

Courtin-Nomade A, Waltzing T, Evrard C et al (2015) Arsenic and lead mobility: from tailing materials to the aqueous compartment. Appl Geochemistry 64:10–21. https://doi.org/10.1016/j.apgeochem.2015.11.002

Degen T, Sadki M, Bron E et al (2014) The HighScore suite. Powder Diffr 29:S13–S18. https://doi.org/10.1017/S0885715614000840

Döbelin N (2021) Profex: open source XRD and Rietveld refinement. https://www.profex-xrd.org/. Accessed 26 Mar 2021

Doebelin N, Kleeberg R (2015) Profex: a graphical user interface for the Rietveld refinement program BGMN. J Appl Crystallogr 48:1573–1580. https://doi.org/10.1107/S1600576715014685

Engstrom DR, Fritz SC, Almendinger JE, Juggins S (2000) Chemical and biological trends during lake evolution in recently deglaciated terrain. Nature 408:161–166. https://doi.org/10.1038/35041500

ESDAC - European Commission (1963) Sveriges Berggrund (Geology Map of Sweden). In: Natl. Soil Maps. https://esdac.jrc.ec.europa.eu/content/sveriges-berggrund-geology-map-sweden. Accessed 28 Dec 2018

Ewing HA, Nater EA (2003) Use of scanning electron microscopy to investigate records of soil weathering preserved in lake sediment. The Holocene 13:51–60. https://doi.org/10.1191/0959683603hl594rp

Feher D (2020) Free World Maps. In: Europe blank maps. https://www.freeworldmaps.net/europe/blank_map.html. Accessed 13 Feb 2020

Felten J, Hall H, Jaumot J et al (2019) Addendum: vibrational spectroscopic image analysis of biological material using multivariate curve resolution–alternating least squares (MCR-ALS). Nat Protoc 14:3032. https://doi.org/10.1038/s41596-019-0196-9

Felten J, Hall H, Jaumot J et al (2015) Vibrational spectroscopic image analysis of biological material using multivariate curve resolution-alternating least squares (MCR-ALS). Nat Protoc 10:217–240. https://doi.org/10.1038/nprot.2015.008

Galán E (2006) Genesis of clay minerals. In: Bergaya F, Theng BKG, Lagaly G (eds) Handbook of clay science. Elsevier Ltd, pp 1129–1162

Gibbard P, Van Kolfschoten T (2004) The Pleistocene and Holocene Epochs. In: Ogg JG, Gradstein FM, Smith AG (eds) A geologic time scale. Cambridge University Press, Cambridge, pp 441–452

Hahn A, Vogel H, Andó S et al (2018) Using Fourier transform infrared spectroscopy to determine mineral phases in sediments. Sediment Geol 375:27–35. https://doi.org/10.1016/j.sedgeo.2018.03.010

Hall AM, Merritt JW, Connell ER, Hubbard A (2019) Early and Middle Pleistocene environments, landforms and sediments in Scotland. Earth Environ Sci Trans R Soc Edinburgh 110:5–37. https://doi.org/10.1017/S1755691018000713

Hanna N, Lartiges B, Kazpard V et al (2018) Hydrogeochemical processes in a small eastern Mediterranean karst watershed (Nahr Ibrahim, Lebanon). Aquat Geochemistry 24:325–344. https://doi.org/10.1007/s10498-018-9346-x

Hillier S (1995) Erosion, sedimentation and sedimentary origin of clays. In: Velde B (ed) Origin and mineralogy of clays. Springer, Berlin Heidelberg, Berlin, Heidelberg, Heidelberg, pp 162–219

Jarman D (2002) Rock slope failure and landscape evolution in the Caledonian mountains, as exemplified in the abisko area, northern sweden. Geogr Ann Ser A, Phys Geogr 84:213–224. https://doi.org/10.1111/j.0435-3676.2002.00176.x

Kalis AJ, Merkt J, Wunderlich J (2003) Environmental changes during the Holocene climatic optimum in central Europe - human impact and natural causes. Quat Sci Rev 22:33–79. https://doi.org/10.1016/S0277-3791(02)00181-6

Kanbar HJ, Kaouk M (2019) Mineral and chemical changes of sediments after Cu sorption and then desorption induced by synthetic root exudate. Chemosphere 236:124393. https://doi.org/10.1016/j.chemosphere.2019.124393

Kanbar HJ, Matar Z, Safa GA-A, Kazpard V (2020a) Selective metal leaching from technosols based on synthetic root exudate composition. J Environ Sci 96:85–92. https://doi.org/10.1016/j.jes.2020.04.040

Kanbar HJ, Montargès-Pelletier E, Losson B et al (2017) Iron mineralogy as a fingerprint of former steelmaking activities in river sediments. Sci Total Environ 599–600:540–553. https://doi.org/10.1016/j.scitotenv.2017.04.156

Kanbar HJ, Olajos F, Englund G, Holmboe M (2020b) Geochemical identification of potential DNA-hotspots and DNA-infrared fingerprints in lake sediments. Appl Geochemistry 122:104728. https://doi.org/10.1016/j.apgeochem.2020.104728

Kullman L (2002) Boreal tree taxa in the central Scandes during the Late-Glacial: implications for Late-Quaternary forest history. J Biogeogr 29:1117–1124. https://doi.org/10.1046/j.1365-2699.2002.00743.x

Laceby JP, McMahon J, Evrard O, Olley J (2015) A comparison of geological and statistical approaches to element selection for sediment fingerprinting. J Soils Sediments 15:2117–2131. https://doi.org/10.1007/s11368-015-1111-9

Lartiges BS, Deneux-Mustin S, Villemin G et al (2001) Composition, structure and size distribution of suspended particulates from the Rhine River. Water Res 35:808–816. https://doi.org/10.1016/S0043-1354(00)00293-1

Lawson S, McGlathery K, Wiberg P (2012) Enhancement of sediment suspension and nutrient flux by benthic macrophytes at low biomass. Mar Ecol Prog Ser 448:259–270. https://doi.org/10.3354/meps09579

Le Meur M, Montargès-Pelletier E, Bauer A et al (2016) Characterization of suspended particulate matter in the Moselle River (Lorraine, France): evolution along the course of the river and in different hydrologic regimes. J Soils Sediments 16:1625–1642. https://doi.org/10.1007/s11368-015-1335-8

Lindholm J, Boily JF, Holmboe M (2019) Deconvolution of smectite hydration isotherms. ACS Earth Sp Chem 3:2490–2498. https://doi.org/10.1021/acsearthspacechem.9b00178

Madejová J, Gates WP, Petit S (2017) IR spectra of clay minerals. In: Gates WP, Kloprogge JT, Madejová J, Bergaya F (eds) Developments in clay science. Eslevier, pp 107–149

Margenot A, Calderón F, Bowles T et al (2015) Soil organic matter functional group composition in relation to organic carbon, nitrogen, and phosphorus fractions in organically managed tomato fields. Soil Sci Soc Am J 79:772–782. https://doi.org/10.2136/sssaj2015.02.0070

Margenot AJ, Parikh SJ, Calderón FJ (2019) Improving infrared spectroscopy characterization of soil organic matter with spectral subtractions. J vis Exp 2019:1–15. https://doi.org/10.3791/57464

Marshak S (2011) Amazing ice: glaciers and ice ages. In: Repcheck J (ed) Earth: portrait of a planet, 2nd edn. W.W. Norton & Company, New York and London, pp 757–800

Meyer-Jacob C, Vogel H, Boxberg F et al (2014) Independent measurement of biogenic silica in sediments by FTIR spectroscopy and PLS regression. J Paleolimnol 52:245–255. https://doi.org/10.1007/s10933-014-9791-5

Mikutta R, Kleber M, Kaiser K, Jahn R (2005) Review: organic matter removal from soils using hydrogen peroxide, sodium hypochlorite, and disodium peroxodisulfate. Soil Sci Soc Am J 69:120. https://doi.org/10.2136/sssaj2005.0120

Mörner NA (2004) Active faults and paleoseismicity in Fennoscandia, especially Sweden. Primary Structures and Secondary Effects Tectonophysics 380:139–157. https://doi.org/10.1016/j.tecto.2003.09.018

Nguyen TT, Janik LJ, Raupach M (1991) Diffuse reflectance infrared Fourier transform (DRIFT) spectroscopy in soil studies. Soil Res 29:49–67. https://doi.org/10.1117/12.970790

Öberg L, Kullman L (2011) Ancient subalpine clonal spruces (Picea abies): sources of postglacial vegetation history in the Swedish scandes. Arctic 64:183–196. https://doi.org/10.14430/arctic4098

Ohfuji H, Rickard DT (2005) Experimental syntheses of framboids—a review. Earth-Science Rev 71:147–170. https://doi.org/10.1016/j.earscirev.2005.02.001

Olajos F, Bokma F, Bartels P et al (2018) Estimating species colonization dates using DNA in lake sediment. Methods Ecol Evol 9:535–543. https://doi.org/10.1111/2041-210X.12890

Olli G (2008) Historic sediment accumulation rates in Karlskärsviken, a bay of Lake Mälaren, Sweden. Hydrol Res 39:123–132. https://doi.org/10.2166/nh.2008.032

Padilla JE, Calderón FJ, Acosta-Martinez V et al (2014) Diffuse-reflectance mid-infrared spectroscopy reveals chemical differences in soil organic matter carried in different size wind eroded sediments. Aeolian Res 15:193–201. https://doi.org/10.1016/j.aeolia.2014.06.003

Panagiotopoulos K, Holtvoeth J, Kouli K et al (2020) Insights into the evolution of the young Lake Ohrid ecosystem and vegetation succession from a southern European refugium during the Early Pleistocene. Quat Sci Rev 227:106044. https://doi.org/10.1016/j.quascirev.2019.106044

Parikh SJ, Goyne KW, Margenot AJ, Calderón FJ (2014) Soil chemical insights provided through vibrational spectroscopy. In: Advances in agronomy. pp 1–148

Pedersen MW, Ginolhac A, Orlando L et al (2013) A comparative study of ancient environmental DNA to pollen and macrofossils from lake sediments reveals taxonomic overlap and additional plant taxa. Quat Sci Rev 75:161–168. https://doi.org/10.1016/j.quascirev.2013.06.006

Pérez CA, Aravena JC, Silva WA et al (2014) Ecosystem development in short-term postglacial chronosequences: N and P limitation in glacier forelands from Santa Inés Island, Magellan Strait. Austral Ecol 39:288–303. https://doi.org/10.1111/aec.12078

Pérez NA, Bucio L, Lima E et al (2016) Identification of allophane and other semi-crystalline and amorphous phases on pre-Hispanic Mexican adobe earth bricks from Cholula, Mexico. Microchem J 126:349–358. https://doi.org/10.1016/J.MICROC.2015.12.033

Poirier V, Basile-Doelsch I, Balesdent J et al (2020) Organo-mineral interactions are more important for organic matter retention in subsoil than topsoil. Soil Syst 4:1–17. https://doi.org/10.3390/soilsystems4010004

Poppe LJ, Paskevich VF, Hathaway JC, Blackwood DS (2001) A laboratory manual for X-ray powder diffraction. U. S. Geological Survey Open-File Report 01–041

Post JE, Bish DL (1989) Rietveld refinement of crystal structures using powder X-ray diffraction data. Mod Powder Diffr 20:277–308

Pulley S, Foster I, Antunes P (2015) The application of sediment fingerprinting to floodplain and lake sediment cores: assumptions and uncertainties evaluated through case studies in the Nene Basin, UK. J Soils Sediments 15:2132–2154. https://doi.org/10.1007/s11368-015-1136-0

Riebe CS, Kirchner JW, Finkel RC (2004) Erosional and climatic effects on long-term chemical weathering rates in granitic landscapes spanning diverse climate regimes. Earth Planet Sci Lett 224:547–562. https://doi.org/10.1016/j.epsl.2004.05.019

Righi D, Meunier A (1995) Origin of clays by rock weathering and soil formation. In: Velde B (ed) Origin and mineralogy of clays. Springer, Berlin Heidelberg, Berlin, Heidelberg, pp 43–161

Rosén P, Vogel H, Cunningham L et al (2010) Fourier transform infrared spectroscopy, a new method for rapid determination of total organic and inorganic carbon and biogenic silica concentration in lake sediments. J Paleolimnol 43:247–259. https://doi.org/10.1007/s10933-009-9329-4

Rydberg J (2014) Wavelength dispersive X-ray fluorescence spectroscopy as a fast, non-destructive and cost-effective analytical method for determining the geochemical composition of small loose-powder sediment samples. J Paleolimnol 52:265–276. https://doi.org/10.1007/s10933-014-9792-4

Sadori L (2013) Pollen records, postglacial | Southern Europe. In: Encyclopedia of quaternary science, 2nd edn. Elsevier B.V., pp 179–188

Schaaf W, Bens O, Fischer A et al (2011) Patterns and processes of initial terrestrial-ecosystem development. J Plant Nutr Soil Sci 174:229–239. https://doi.org/10.1002/jpln.201000158

Schnurrenberger D, Russell J, Kelts K (2003) Classification of lacustrine sediments based on sedimentary components. J Paleolimnol 29:141–154. https://doi.org/10.1023/A:1023270324800

SGU (2019) Sveriges geologiska undersökning. In: Berggrund 11 miljon. Bedrock 11 million (in English). https://apps.sgu.se/kartvisare/kartvisare-berggrund-1-miljon.html. Accessed 22 May 2019

Snowball I, Zillén L, Gaillard MJ (2002) Rapid early-Holocene environmental changes in northern Sweden based on studies of two varved lake-sediment sequences. Holocene 12:7–16. https://doi.org/10.1191/0959683602hl515rp

Strakhovenko V, Subetto D, Ovdina E et al (2020) Mineralogical and geochemical composition of Late Holocene bottom sediments of Lake Onego. J Great Lakes Res 46:443–455. https://doi.org/10.1016/j.jglr.2020.02.007

Stroeven AP, Hättestrand C, Kleman J et al (2016) Deglaciation of Fennoscandia. Quat Sci Rev 147:91–121. https://doi.org/10.1016/j.quascirev.2015.09.016

Swärd H, O'Regan M, Björck S et al (2018) A chronology of environmental changes in the Lake Vättern basin from deglaciation to its final isolation. Boreas 47:609–624. https://doi.org/10.1111/bor.12288

Thorpe MT, Hurowitz JA (2020) Unraveling sedimentary processes in fluvial sediments from two basalt dominated watersheds in northern Idaho, USA. Chem Geol 550:119673. https://doi.org/10.1016/j.chemgeo.2020.119673

Thorpe MT, Hurowitz JA, Dehouck E (2019) Sediment geochemistry and mineralogy from a glacial terrain river system in southwest Iceland. Geochim Cosmochim Acta 263:140–166. https://doi.org/10.1016/j.gca.2019.08.003

Tombácz E, Libor Z, Illés E et al (2004) The role of reactive surface sites and complexation by humic acids in the interaction of clay mineral and iron oxide particles. Org Geochem 35:257–267. https://doi.org/10.1016/j.orggeochem.2003.11.002

Tombácz E, Szekeres M (2006) Surface charge heterogeneity of kaolinite in aqueous suspension in comparison with montmorillonite. Appl Clay Sci 34:105–124. https://doi.org/10.1016/j.clay.2006.05.009

Tran D, Strom K (2019) Floc sizes and resuspension rates from fresh deposits: influences of suspended sediment concentration, turbulence, and deposition time. Estuar Coast Shelf Sci 229:106397. https://doi.org/10.1016/j.ecss.2019.106397

Velde B, Meunier A (2008) Basics for the study of soil and weathered rock geochemical systems. In: The origin of clay minerals in soils and weathered rocks. Springer, pp 75–111

Vogel H, Meyer-Jacob C, Thöle L et al (2016) Quantification of biogenic silica by means of Fourier transform infrared spectroscopy

(FTIRS) in marine sediments. Limnol Oceanogr Methods 14:828–838. https://doi.org/10.1002/lom3.10129

Voldstad LH, Alsos IG, Farnsworth WR et al (2020) A complete Holocene lake sediment ancient DNA record reveals long-standing high Arctic plant diversity hotspot in northern Svalbard. Quat Sci Rev 234:106207. https://doi.org/10.1016/j.quascirev.2020.106207

Zale R, Huang YT, Bigler C et al (2018) Growth of plants on the Late Weichselian ice-sheet during Greenland interstadial-1? Quat Sci Rev 185:222–229. https://doi.org/10.1016/j.quascirev.2018.02.005

Zhou X, Liu D, Bu H et al (2018) XRD-based quantitative analysis of clay minerals using reference intensity ratios, mineral intensity factors, Rietveld, and full pattern summation methods: a critical review. Solid Earth Sci 3:16–29. https://doi.org/10.1016/j.sesci.2017.12.002

Zimmermann-Timm H (2002) Characteristics, dynamics and importance of aggregates in rivers - an invited review. Int Rev Hydrobiol 87:197–240. https://doi.org/10.1002/1522-2632(200205)87:2/3%3c197::AID-IROH197%3e3.0.CO;2-7

Zimmermann HH, Stoof-Leichsenring KR, Kruse S et al (2021) Sedimentary ancient DNA from the Subarctic North Pacific: how sea ice, salinity, and insolation dynamics have shaped diatom composition and richness over the past 20,000 years. Paleoceanogr Paleoclimatology. https://doi.org/10.1029/2020PA004091